






An Early Transition to Magnetic Supercriticality in Star Formation

T.-C. Ching¹ , D. Li^{1,2,3} *, C. Heiles⁴, Z.-Y. Li⁵, L. Qian¹ , Y. L. Yue¹ , J. Tang¹ , S. H. Jiao^{1,2}

¹*National Astronomical Observatories, Chinese Academy of Sciences, Beijing 100101, China*

²*Department of Astronomy, University of Chinese Academy of Sciences, Beijing 100049, China*

³*NAOC-UKZN Computational Astrophysics Centre, University of KwaZulu-Natal, Durban 4000, South Africa*

⁴*Department of Astronomy, University of California, Berkeley, CA 94720, USA*

⁵*Astronomy Department, University of Virginia, Charlottesville, VA 22904, USA*

Magnetic fields play an important role in the evolution of interstellar medium and star formation^{1,2}. As the only direct probe of interstellar field strength, credible Zeeman measurements remain sparse due to the lack of suitable Zeeman probes, particularly for cold, molecular gas³. Here we report the detection of a magnetic field of $+3.8 \pm 0.3 \mu\text{G}$ through the H_I narrow self-absorption (H_INSA)^{4,5} toward L1544^{6,7}, a well-studied prototypical prestellar core in an early transition between starless and protostellar phases^{8–10} characterized by high central number density¹¹ and low central temperature¹². A combined analysis of the Zeeman measurements of quasar H_I absorption, H_I emission, OH emission, and H_INSA reveals a coherent magnetic field from the atomic cold neutral medium (CNM) to the molecular en-

*Email:dili@nao.cas.cn, orcid.org/0000-0003-3010-7661

velope. The molecular envelope traced by H_INSA is found to be magnetically supercritical, with a field strength comparable to that of the surrounding diffuse, magnetically subcritical CNM despite a large increase in density. The reduction of the magnetic flux relative to the mass, necessary for star formation, thus seems to have already happened during the transition from the diffuse CNM to the molecular gas traced by H_INSA , earlier than envisioned in the classical picture where magnetically supercritical cores capable of collapsing into stars form out of magnetically subcritical envelopes^{13,14}.

In non-masing interstellar medium, only H_I, OH, and CN have successfully produced systematic Zeeman measurements. The comprehensive Zeeman surveys¹⁵ indicate that the magnetic fields in diffuse CNM probed by H_I do not scale significantly with density, whereas above a critical break-point density $\sim 300 \text{ cm}^{-3}$, the magnetic fields in dense cores probed by OH tend to increase with density. However, owing to the gap in densities between the H_I ($\sim 40 \text{ cm}^{-3}$) and OH ($\gtrsim 10^3 \text{ cm}^{-3}$) Zeeman measurements, the field transition around the critical density of $\sim 300 \text{ cm}^{-3}$ (where the dependence of the field strength on the density changes behavior) remains a controversial topic and could have crucial implication on star formation¹⁶⁻¹⁹. Recently, a CCS Zeeman detection²⁰ sheds light into regions denser than that probed by OH. A Zeeman probe sensitive for a wide range of densities, particularly the low-density molecular envelope, is highly desirable and could help to distinguish different core formation scenarios.

We developed the so-called H_INSA technique to provide a probe of the transition from H_I to H₂^{4,5}. H_INSA traces cold atomic hydrogen well mixed with H₂, which provides the necessary cool-

ing, not available in the CNM, of H_I through collision. Close to the steady state between H₂ formation and destruction, the H_INSA strength is independent of the gas density⁵, and thus capable of probing the transition around the critical density. Although the Zeeman effect of H_I self-absorption feature has been reported^{21,22}, the broad line widths of the absorption components are mostly associated with diffuse atomic gas rather than dense molecular gas. Considering that H_INSA typically has much higher brightness temperatures than most molecular lines, impervious to depletion²³, and can be detected in a wide range of H₂ densities, H_INSA is a promising Zeeman probe for molecular gas.

The H_INSA feature in L1544 has a strong absorption dip and a nearly thermalized narrow line width at a temperature lower than 15 K⁴. The non-thermal line width and centroid velocity of the H_INSA are very close to those of the emission lines of OH, ¹³CO, and C¹⁸O molecules, and their column densities are well correlated, suggesting that a significant fraction of the atomic hydrogen is located in the cold, well-shielded portions of L1544⁵. We thus assume that the column density sampled by the H_INSA can be approximated by that obtained from dust, despite the substantially larger apparent area covered by H_INSA (Fig. 1a). The previous OH Zeeman detection with Arecibo²⁴ toward the L1544 center resulted in a field strength of $B_{los} = +10.8 \pm 1.7 \mu\text{G}$, where B_{los} is the magnetic field component along the line of sight with positive sign representing field pointing away from the observer. In contrast, the OH Zeeman observations of the Green Bank Telescope (GBT) toward four envelope locations 6.0' (0.24 pc) from the center yielded a marginal detection $B_{los} = +2 \pm 3 \mu\text{G}$ ¹⁶, leaving the structure of envelope field undetermined.

With the Five-hundred-meter Aperture Spherical radio Telescope (FAST)²⁵, we detected Zeeman splittings in a 2.9' beam (0.12 pc) toward the HiNSA column density peak, 3.6' (0.15 pc) away from the L1544 center (Fig. 1). The spectra of the Stokes $I(\nu)$ and $V(\nu)$ parameters (where ν denotes velocity) are shown in Fig. 2. The $I(\nu)$ spectrum contains H I emission of CNM and warm neutral medium (WNM) clouds in the direction toward the Taurus complex and a HiNSA feature at the centroid velocity of L1544. Fig. 2a shows our decomposition of $I(\nu)$ into a foreground HiNSA component, a background WNM component, and three CNM components between the HiNSA and WNM. Our fitted parameters of the HiNSA component are in good agreement with the previous HiNSA observations^{4,5}, and our parameters of the CNM and WNM components are similar to the Arecibo results toward quasars around L1544²⁶.

The $V(\nu)$ spectrum shows features of classic 'S curve' patterns proportional to the first derivatives of $I(\nu)$ for the HiNSA, CNM, and WNM components, as expected for Zeeman splittings. The Zeeman splitting profile of HiNSA has a maximum at high velocity and a minimum at low velocity, opposite to the Zeeman splitting profile of CNM1, the closest CNM component at a velocity similar to L1544, that shows positive V at low velocity and negative V at high velocity. From our least-squares fits to $V(\nu)$, Fig. 2b shows the Zeeman splitting of the HiNSA and the total Zeeman profile of the five components, and Fig. 3 shows the individual Zeeman splittings and B_{los} of the components. The HiNSA Zeeman effect gives $B_{los} = +3.8 \pm 0.3 \mu\text{G}$, and the Hi Zeeman effect of CNM1 gives $B_{los} = +4.0 \pm 1.1 \mu\text{G}$. The magnetic field strengths of HiNSA and CNM1 are consistent with the results of $B_{los} = +5.8 \pm 1.1 \mu\text{G}$ and $+4.2 \pm 1.0 \mu\text{G}$ obtained from the Zeeman observations toward quasars 3C133 and 3C132, probing the magnetic fields of CNM1 at distances

of $17.7'$ (0.72 pc) and $174.5'$ (7.1 pc) from L1544, respectively²⁷. For the second and third CNM components (CNM2 and CNM3) along the line of sight, our results of $B_{los,CNM2} = -7.6 \pm 1.0 \mu\text{G}$ and $B_{los,CNM3} = +2.9 \pm 0.4 \mu\text{G}$ are also consistent with the results of $B_{los,CNM2} = -9.6 \pm 6.3 \mu\text{G}$ and $B_{los,CNM3} = -0.3 \pm 1.7 \mu\text{G}$ toward quasar 3C133²⁷.

Comparing the Zeeman observations of H_INSA, OH, and H_I tracing the CNM1 and the molecular envelope of L1544, it is clear that the magnetic fields at distances of 0.15, 0.24, 0.72, and 7.1 pc from the center all have the same direction of B_{los} and consistent strengths roughly within the 1σ . This finding is in agreement with the conclusion of a median value of $6 \mu\text{G}$ in absolute total strength in H_I clouds inferred from comprehensive Zeeman surveys¹⁵. H_INSA Zeeman effect thus provides a connection between the magnetic fields from H_I clouds to molecular clouds. The HI emission components (CNM1, CNM2, CNM3) and the H_I absorption toward 3C133 and 3C132 trace CNM with a kinematic temperature of about 100 K ²⁷ and a number density of about 40 cm^{-3} ¹⁵, whereas the H_INSA and OH observations trace the envelope of about $10\text{--}15 \text{ K}$ ⁴ and $\sim 10^3 \text{ cm}^{-3}$ ^{5,15}. Despite the 1-2 orders of magnitude change in both temperature and density in the phase transition from the atomic CNM to the molecular envelope, the Zeeman observations reveal a magnetic field that is coherent in both direction and strength across multi-scales and multi-phases of the interstellar medium. To constrain the uniformity of the coherent magnetic field, our likelihood analysis of the H_INSA, OH, and H_I Zeeman measurements suggests a gaussian distribution of the B_{los} with a mean strength of $B_0 = +4.1 \pm 1.6 \mu\text{G}$ and an intrinsic spread of $\sigma_0 = 1.2_{-0.6}^{+1.2} \mu\text{G}$, a significantly better constraint than the previous estimation of $B_0 = +4_{-8}^{+10} \mu\text{G}$ based only on the OH results¹⁸.

It is well known that the progenitor of molecular gas, the atomic CNM, is strongly magnetized, as measured by the dimensionless mass-to-magnetic flux ratio λ in units of the critical value of $2\pi G^{1/2}$ ($\lambda = 7.6 \times 10^{-21} [N_{H_2}/\text{cm}^{-2}][B_{tot}/\mu\text{G}]^{-1}$, where N_{H_2} is the column density of H_2 gas and B_{tot} is the total magnetic field strength¹), which is well below unity (i.e., magnetically subcritical)²⁸. On the other hand, the immediate progenitors of stars, the prestellar cores of molecular clouds such as the L1554 core, are observed to be magnetically supercritical ($\lambda > 1$)²⁴, which is required for the self-gravity to overwhelm the magnetic support and form stars through gravitational collapse. When and how the transition from the magnetically subcritical CNM that is incapable of forming stars through direct gravitational collapse to the supercritical star-forming cores occurs is a central unresolved question in star formation.

Our HiNSA Zeeman observations can be used to address this question. Using the physical parameters of the clouds (Table 1) and the statistically most probable value of $B_{tot} = 2B_{los}$, the λ of CNM1 is about 0.10–0.18, consistent with previous results²⁸. The λ of the envelope and core of L1544 core is 2.5–3.5, which is well above unity, indicating that the transition to magnetic supercriticality has already occurred. We further consider the relative values of λ between CNM1 and L1544 to avoid the geometrical correction from B_{los} to B_{tot} ¹⁶, assuming that the inclination angles of the magnetic fields in the L1544 core and envelope are similar. Therefore, the molecular envelope of the L1544 core traced by HiNSA is at least 13 times less magnetized relative to its mass compared to its ambient CNM. This is different from the “classic” theory of low-mass star formation, which envisions the transition from magnetic subcriticality to supercriticality occurring as the supercritical core forms out of the magnetically supported (subcritical) envelope^{13,14}. Our results

suggest that the transition from magnetic subcriticality to supercriticality occurs earlier, during the formation of the molecular envelope, favoring the more rapidly evolving scenario of core formation and evolution for L1544⁸ over the slower, magnetically retarded scenario⁹. In other words, by the time that the molecular envelope is formed, the problem of excessive magnetic flux as a fundamental obstacle to gravitational collapse and star formation is already resolved. This early reduction of flux relative to mass is unlikely due to the “classical” scenario where gravity drives neutrals through ions (and the magnetic field tied to them) in a process called “ambipolar diffusion” because the CNM is not self-gravitating. The coherent magnetic fields reviewed here provide a new specific question on how to create supercritical dense cores such as L1544 from subcritical clouds. Plausible scenarios include mass accumulation along field lines²⁹ and (turbulence-enhanced) magnetic reconnection³⁰, although whether such scenarios can reproduce the distributions of gas and magnetic field observed in the L1544 region remains to be seen. In any case, the already magnetically supercritical envelope can in principle go on to form dense cores and stars without having to further reduce its magnetic flux relative to the mass.

1. McKee, C. F. & Ostriker, E. C. Theory of Star Formation. Annu. Rev. Astron. Astrophys. **45**, 565–687 (2007).
2. Hennebelle, P. & Inutsuka, S.-i. The role of magnetic field in molecular cloud formation and evolution. Front. Astron. Space Sci. **6**, 5 (2019).
3. Crutcher, R. M. & Kemball, A. J. Review of Zeeman Effect Observations of Regions of Star Formation. Front. Astron. Space Sci. **6**, 66 (2019).

4. Li, D. & Goldsmith, P. F. H I Narrow Self-Absorption in Dark Clouds. *Astrophys. J.* **585**, 823–839 (2003).
5. Goldsmith, P. F. & Li, D. H I Narrow Self-Absorption in Dark Clouds: Correlations with Molecular Gas and Implications for Cloud Evolution and Star Formation. *Astrophys. J.* **622**, 938–958 (2005).
6. Elias, J. H. A study of the Taurus dark cloud complex. *Astrophys. J.* **224**, 857–872 (1978).
7. Tafalla, M. et al. L1544: A Starless Dense Core with Extended Inward Motions. *Astrophys. J.* **504**, 900–914 (1998).
8. Aikawa, Y., Ohashi, N., Inutsuka, S.-i., Herbst, E. & Takakuwa, S. Molecular Evolution in Collapsing Prestellar Cores. *Astrophys. J.* **552**, 639–653 (2001).
9. Li, Z.-Y., Shematovich, V. I., Wiebe, D. S. & Shustov, B. M. A Coupled Dynamical and Chemical Model of Starless Cores of Magnetized Molecular Clouds. I. Formulation and Initial Results. *Astrophys. J.* **569**, 792–802 (2002).
10. Keto, E., Caselli, P. & Rawlings, J. The dynamics of collapsing cores and star formation. *Mon. Not. R. Astron. Soc.* **446**, 3731–3740 (2015).
11. Caselli, P. et al. The Central 1000 au of a Pre-stellar Core Revealed with ALMA. I. 1.3 mm Continuum Observations. *Astrophys. J.* **874**, 89 (2019).

12. Crapsi, A., Caselli, P., Walmsley, M. C. & Tafalla, M. Observing the gas temperature drop in the high-density nucleus of L 1544. *Astron. Astrophys.* **470**, 221–230 (2007).
13. Shu, F. H., Adams, F. C. & Lizano, S. Star formation in molecular clouds: observation and theory. *Annu. Rev. Astron. Astrophys.* **25**, 23–81 (1987).
14. Mouschovias, T. C. & Ciolek, G. E. Magnetic Fields and Star Formation: A Theory Reaching Adulthood. In Lada, C. J. & Kylafis, N. D. (eds.) *The Origin of Stars and Planetary Systems*, vol. 540 of *NATO Advanced Study Institute (ASI) Series C*, 305–340 (1999).
15. Crutcher, R. M., Wandelt, B., Heiles, C., Falgarone, E. & Troland, T. H. Magnetic Fields in Interstellar Clouds from Zeeman Observations: Inference of Total Field Strengths by Bayesian Analysis. *Astrophys. J.* **725**, 466–479 (2010).
16. Crutcher, R. M., Hakobian, N. & Troland, T. H. Testing Magnetic Star Formation Theory. *Astrophys. J.* **692**, 844–855 (2009).
17. Crutcher, R. M., Hakobian, N. & Troland, T. H. Self-consistent analysis of OH Zeeman observations. *Mon. Not. R. Astron. Soc.* **402**, L64–L66 (2010).
18. Mouschovias, T. C. & Tassis, K. Testing molecular-cloud fragmentation theories: self-consistent analysis of OH Zeeman observations. *Mon. Not. R. Astron. Soc.* **400**, L15–L19 (2009).
19. Mouschovias, T. C. & Tassis, K. Self-consistent analysis of OH-Zeeman observations: too much noise about noise. *Mon. Not. R. Astron. Soc.* **409**, 801–807 (2010).

20. Nakamura, F. et al. First clear detection of the CCS Zeeman splitting toward the pre-stellar core, Taurus Molecular Cloud 1. Publ. Astron. Soc. Jpn. **71**, 117 (2019).
21. Goodman, A. A. & Heiles, C. The Magnetic Field in the Ophiuchus Dark Cloud Complex. Astrophys. J. **424**, 208–221 (1994).
22. Heiles, C. A Holistic View of the Magnetic Field in the Eridanus/Orion Region. Astrophys. J. Suppl. Ser. **111**, 245–288 (1997).
23. Goldsmith, P. F., Li, D. & Krčo, M. The Transition from Atomic to Molecular Hydrogen in Interstellar Clouds: 21 cm Signature of the Evolution of Cold Atomic Hydrogen in Dense Clouds. Astrophys. J. **654**, 273–289 (2007).
24. Crutcher, R. M. & Troland, T. H. OH Zeeman Measurement of the Magnetic Field in the L1544 Core. Astrophys. J. Lett. **537**, L139–L142 (2000).
25. Li, D. et al. FAST in Space: Considerations for a Multibeam, Multipurpose Survey Using China’s 500-m Aperture Spherical Radio Telescope (FAST). IEEE Microw. Mag. **19**, 112–119 (2018).
26. Heiles, C. & Troland, T. H. The Millennium Arecibo 21 Centimeter Absorption-Line Survey. I. Techniques and Gaussian Fits. Astrophys. J. Suppl. Ser. **145**, 329–354 (2003).
27. Heiles, C. & Troland, T. H. The Millennium Arecibo 21 Centimeter Absorption-Line Survey. III. Techniques for Spectral Polarization and Results for Stokes V. Astrophys. J. Suppl. Ser. **151**, 271–297 (2004).

28. Heiles, C. & Troland, T. H. The Millennium Arecibo 21 Centimeter Absorption-Line Survey. IV. Statistics of Magnetic Field, Column Density, and Turbulence. *Astrophys. J.* **624**, 773–793 (2005).
29. Vázquez-Semadeni, E. *et al.* Molecular cloud evolution - IV. Magnetic fields, ambipolar diffusion and the star formation efficiency. *Mon. Not. R. Astron. Soc.* **414**, 2511–2527 (2011).
30. Lazarian, A., Esquivel, A. & Crutcher, R. Magnetization of Cloud Cores and Envelopes and Other Observational Consequences of Reconnection Diffusion. *Astrophys. J.* **757**, 154 (2012).

Table 1: **Physical Parameters of the Clouds**

Tracer/Cloud	B_{los} [μG]	N_{H_2} [10^{20} cm^{-2}]	$\lambda^{\dagger\dagger}$
H _{13C132} /CNM1	$+4.2 \pm 1.0$	2.03 ± 0.54 [†]	0.18 ± 0.07
H _{13C133} /CNM1	$+5.8 \pm 1.1$	1.45 ± 0.52 [†]	0.10 ± 0.04
H ₁ NSA/envelope	$+3.8 \pm 0.3$	34.9 ± 0.1 [‡]	3.5 ± 0.3
OH/core	$+10.8 \pm 1.7$	70.5 ± 0.2 [‡]	2.5 ± 0.4

[†] Equivalent H₂ column density obtained from the H₁ column density listed in Ref. 26.

[‡] Obtained from the H₂ column density map in Fig. 1a. The N_{H_2} of the core is consistent with the value of $\sim 9 \times 10^{21} \text{ cm}^{-2}$ estimated based on OH abundance¹⁶.

^{††} Obtained with $B_{tot} = 2B_{los}$.

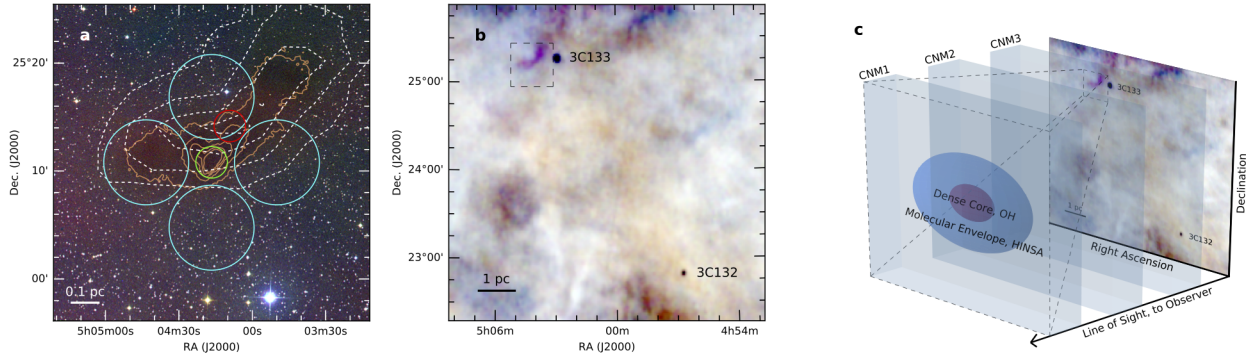


Figure 1: **L1544 core and illustration of the structure of interstellar medium from CNM to core.** **a**, a composite of DSS2 images of L1544 with *i*-band in red, *r*-band in green, and *b*-band in blue overlaid with H I N S A and H₂ column density maps. White dashed contours are 30%, 50%, 70%, and 90% of the peak H I N S A column density, and orange contours are 2, 4, 6, 8, 10 × 10²¹ cm⁻² for the H₂ column density. The red, green, and cyan circles mark the locations and beam sizes of the FAST, Arecibo, and GBT Zeeman observations, respectively. **b**, a composite of three 0.5 km s⁻¹ velocity slices of Arcibo GALFA-H I images at 6.2, 6.7, and 7.3 km s⁻¹ LSR velocities in blue, green, and red. The dashed rectangle shows the region of **a**. The two absorption dots represent the locations of quasars 3C132 and 3C133. **c**, schematic view of CNMs, molecular envelope, and L1544 core.

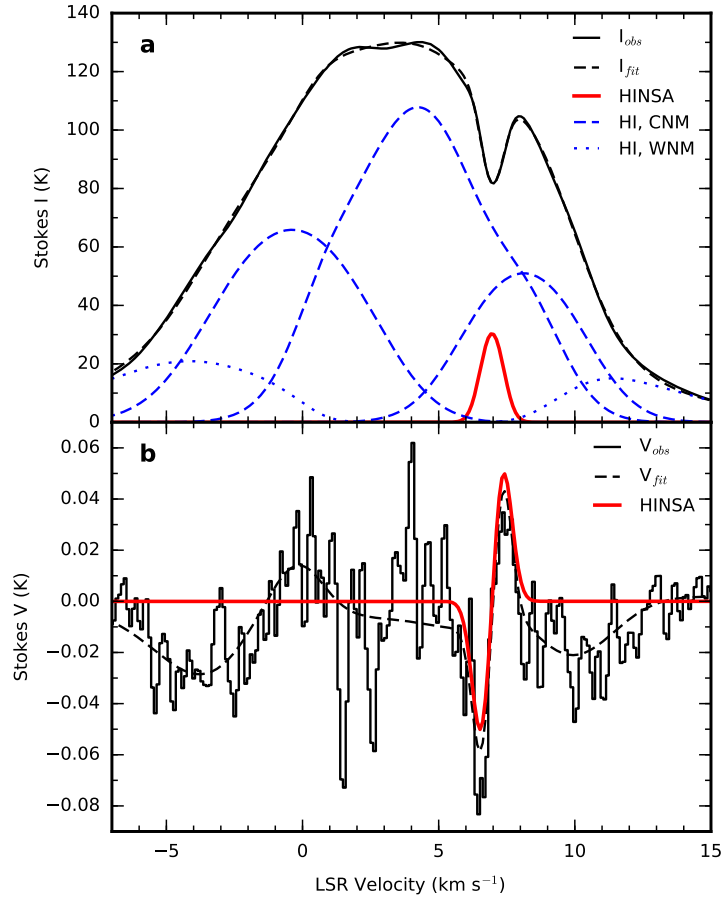


Figure 2: **The Stokes $I(v)$ and $V(v)$ spectra at 21-cm wavelength toward the HiNSA column density peak.** **a**, The black profile represents the $I(v)$ spectrum. The red profile represents the absorption from the foreground HiNSA component. The blue dashed and dotted profiles represent the emission of the CNM and WNM components, respectively. The CNM and WNM profiles include the absorption from the CNM components that lie in front but not include the absorption from HiNSA. The black dashed profile represents the sum of the absorption and emission profiles. **b**, The black profile represents the $V(v)$ spectrum. The black dashed profile represents the sum of the Zeeman splitting profiles of the five components. The red profile represents the Zeeman splitting profile with $B_{los} = +3.8 \mu\text{G}$ of the HiNSA component.

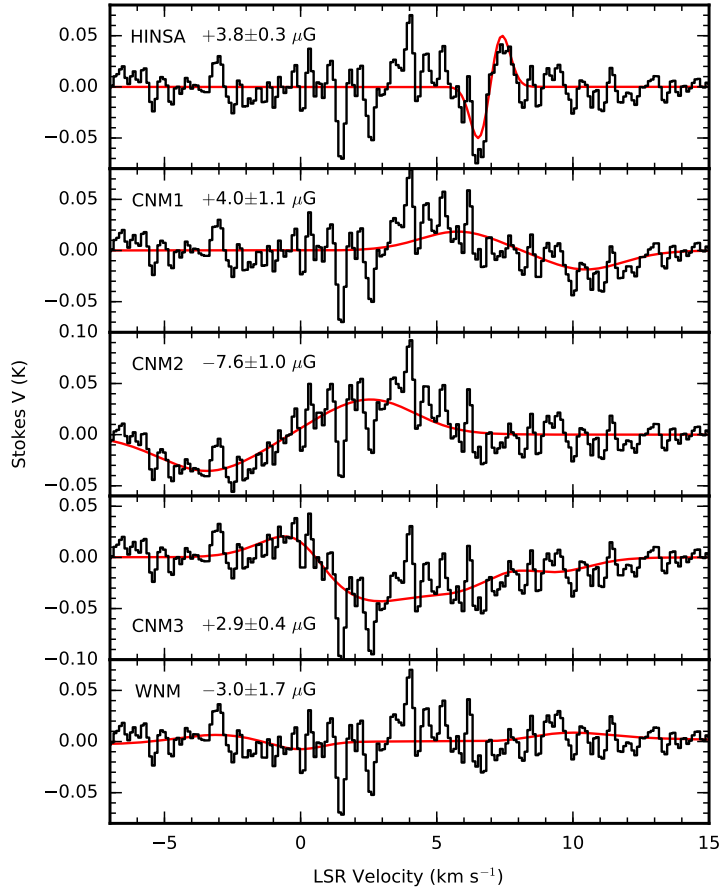


Figure 3: **The individual $V(v)$ profiles for the HINSA , CNM, and WNM components.** In each panel, the red profile represents the fitted Zeeman profile of the component, and the black profile represents the observed $V(v)$ subtracted by the fitted Zeeman profiles of the other four components. The CNM and WNM Zeeman profiles include the absorption from the CNM components that lie in front but not include the absorption from HINSA . The sum of the red profiles of the five components is the black dashed profile in Fig. 2b.

Methods

Data reduction The FAST Zeeman observations toward the H_INSA column density peak in L1544 were carried out on five days between August and November of 2019 with a total integration time of 7.6 hours. The H_INSA spectra were obtained with the central beam of the *L*-band 19-beam receiver³¹. The central beam has an average system temperature of 24 K, a main beam efficiency of 0.63, and a main beam diameter at the half-power point of 2.9' with a pointing accuracy of 7.9". The 19-beam receiver had orthogonal linear polarization feeds followed by a temperature stabilized noise injection system and low noise amplifiers to produce the X and Y signals of the two polarization paths. The XX, YY, XY, and YX correlations of the signals then were simultaneously recorded using the ROACH backend with 65536 spectral channels in each polarization. The spectral bandwidth was 32.75 MHz centered at the frequency of the H_I 21-cm line for a channel spacing of 500 Hz, and the $V(\nu)$ spectrum presented in this work was Hanning-smoothed, which produced a spectral resolution of 0.21 km s⁻¹.

The data reduction including gain and phase calibrations of the two polarization paths, band-pass calibrations of the four correlated spectra, and polarization calibrations to generate Stokes I , Q , U , and V spectra was made with the IDL RHSTK package written by C. Heiles and T. Robishaw that is widely used for Arecibo and GBT polarization data. The 19-beam receiver is rotatable from -80° to +80° with respect to the line of equatorial latitude. The polarization calibrations used drifting scans of the continuum source 3C286 at rotation angles of -60°, -30°, 0°, 30°, and 60° over 1.5 hours surrounding its transit. The details of the polarization calibration procedure were provided in³². We performed polarization calibrations once a month during the observations. The calibrated

polarization of 3C286 of the three epochs were $8.9\% \pm 0.1\%$, $8.7\% \pm 0.2\%$, and $9.0\% \pm 0.1\%$ for polarization degrees and $30.4^\circ \pm 0.3^\circ$, $33.8^\circ \pm 0.5^\circ$, and $29.4^\circ \pm 0.3^\circ$ for polarization angles. Considering that the ionosphere can generate a faraday rotation of $1^\circ\text{--}3^\circ$ in polarization angle at L -band³³, our results were consistent with the intrinsic polarization degree of 9.5% and polarization angle of 33° of 3C286 at 1450 MHz³⁴. In addition to the polarization observations of L1544 and 3C286, we observed the circularly polarized OH maser source IRAS02524+2046³⁵ in order to verify that our procedures produced consistent B_{los} , including the sign or direction of the magnetic field, as had been obtained previously.

The convolutions of the sidelobes of the Stokes V beam with the spatial gradient of the Stokes I emission may generate a false ‘S curve’ in the V spectrum²⁷. In order to check the credibility of our Zeeman detections, we measured the Stokes V beam of FAST and convolved the beam with the GALFA Stokes I cube³⁶ of L1544. The convolved V spectrum showed a profile with a shape similar to the I spectrum and a strength less than 0.03% of the I spectrum, different from the ‘S curve’ patterns in the observed V spectrum. Meanwhile, the 19-beam receiver was rotated to -45° , 0° , and 45° in the three epochs of the L1544 observations, and all of the three epochs showed ‘S curve’ patterns in the V spectra, indicating that our Zeeman results were true detections.

Although the data of the 19 beams of the FAST L -band receiver were simultaneously taken in our observations, only the polarization of the central beam were commissioned at the time of writing. The results represented in this work were made with only the central beam pointing toward the H_INSA column density peak in Fig. 1. The Zeeman results of the 18 off-central beams will be published in the future.

Multiple gaussians and radiative transfer fitting to $I(\nu)$ and $V(\nu)$ We adopts the least-squares fits of multiple gaussians with radiative transfer²⁶ to decompose the $I(\nu)$ into HiNSA , CNM, and WNM components. The expected profile of $I(\nu)$ consists of multiple CNM components providing opacity and also brightness temperature and a WNM component providing only brightness temperature:

$$I(\nu) = I_{CNM}(\nu) + I_{WNM}(\nu). \quad (1)$$

The $I_{CNM}(\nu)$ is an assembly of N CNM components

$$I_{CNM}(\nu) = \sum_{n=1}^N I_{peak,n} (1 - e^{-\tau_n(\nu)}) e^{-\sum_{m=1}^M \tau_m(\nu) + \tau_0}, \quad (2)$$

where the subscript m with its associated optical depth profile $\tau_m(\nu)$ represents each of the M CNM clouds that lie in front of cloud n . The optical depth of the i th component is

$$\tau_i(\nu) = \tau_i e^{-[(\nu - \nu_{0,i})/\sigma_{\nu,i}]^2} \quad (3)$$

in which τ_0 represents the HiNSA providing only opacity and no brightness temperature. For the WNM in the background,

$$I_{WNM}(\nu) = I_{peak,WNM} e^{-[(\nu - \nu_{0,WNM})/\sigma_{\nu,WNM}]^2} e^{-\sum_{i=0}^N \tau_i(\nu)}. \quad (4)$$

The fitting of $I(\nu)$ thus yields values for I_{peak} , τ , ν_0 , and σ_ν of the components.

We consider the radiative transfer of $V(\nu)$ in terms of right circular polarization (RCP) and left circular polarization (LCP). The Zeeman effect states that with the existence of B_{los} , the frequency of RCP shifts from its original frequency ν_0 to $\nu_0 + \nu_z$ and the frequency of LCP shifts to $\nu_0 - \nu_z$ with $\nu_z = (Z/2) \times B_{los}$, where Z is the Zeeman splitting factor ($2.8 \text{ Hz } \mu\text{G}^{-1}$ for H α 21-cm line). Since the RCP and LCP are orthogonal components of radiation, the radiative transfer

processes of RCP and LCP are independent to each other. For RCP, Equation (1) becomes

$$T_{RCP} = T_{RCP,CNM}(v, \tau_{RCP,i}) + T_{RCP,WNM}(v, \tau_{RCP,i}), \quad (5)$$

where for the i th component, $T_{RCP,i} = I_{peak,i}/2$, $\tau_{RCP,i}$ is optical depth in the RCP radiation to substitute the τ_i in Equation (3) with $\tau_{RCP,i} = \tau_i(v_0 + v_{z,i})$ for $B_{los,i}$ of the component, and the parameters of v_0 and σ_v keep the same. Similarly, for LCP,

$$T_{LCP} = T_{LCP,CNM}(v, \tau_{LCP,i}) + T_{LCP,WNM}(v, \tau_{LCP,i}) \quad (6)$$

with $T_{LCP,i} = I_{peak,i}/2$ and $\tau_{LCP,i} = \tau_i(v_0 - v_{z,i})$. The fitting of $V(v) = T_{RCP} - T_{LCP} + cI(v)$, which includes a c term accounting for leakage of $I(v)$ into $V(v)$, thus yields values for B_{los} of the components. In Extended Data Table 1, we list the parameters of the components obtained from least-squares fits to $I(v)$ and $V(v)$. The leakage of our HiNSA Zeeman observations is $c = 0.034\%$.

HiNSA and H₂ column density maps L1544 is a low-mass prestellar core in the Taurus molecular cloud complex at a distance of about 140 pc. The core has a size of ~ 0.1 pc³⁷, presumably formed out of a parsec-long elongated molecular ridge⁷ which, for simplicity, we refer as the molecular envelope. We show the HiNSA and H₂ column density maps of L1544 in Fig. 1a, and we use the H₂ column density map to calculate the N_{H_2} of the envelope and core at the beams of FAST and Arecibo observations in Table 1. The HiNSA column density map is a revision of the Fig. 8 in Ref. 4. To derive the H₂ column density map, we retrieved the level 2.5 processed, archival Herschel images that were taken at 250/350/500 μm using the SPIRE instrument³⁸, (obsID: 1342204842). We smoothed the Herschel images to a common angular resolution of the 36'' beam at 500 μm and regridded the images to the same pixel size of 6''. We performed least-squares

fits of the 250/350/500 μm spectral energy distributions weighted by the squares of the measured noise levels to derive the pixel-to-pixel distributions of dust temperature T_d and dust optical depth τ_ν using $S_\nu = \Omega_m B_\mu(T_d)(1 - e^{-\tau_\nu})$, where S_ν is the flux density at frequency ν , Ω_m is the solid angle of the pixel, $B_\mu(T_d)$ is the Planck function at T_d , and $\tau_\nu = \tau_{230}(\nu[\text{GHz}]/230)^\beta$ with dust opacity index β of 1.8. Next, we obtained the H_2 column density with $N_{\text{H}_2} = g\tau_{230}/(\kappa_{230}\mu_m m_H)$, where $g = 100$ is the gas-to-dust mass ratio, $\kappa_{230} = 0.09 \text{ cm}^2 \text{ g}^{-2}$ ³⁹ is the dust opacity at 230 GHz, $\mu_m = 2.8$ is the mean molecular weight, and m_H is the atomic mass of hydrogen. To estimate the uncertainties in the H_2 column density, we used a Monte-Carlo technique. For each pixel, we created artificial 250/350/500 μm flux densities by adding the original flux densities with normal-distributed errors taking account the uncertainty in the measured flux and a 10% correlation for the calibration uncertainty in SPIRE⁴⁰. We then estimated the uncertainty in each pixel with 1000 fittings of the H_2 column density. The N_{H_2} and its uncertainty in Table 1 were obtained from the convolutions of the H_2 column density map and uncertainty map with the FAST and Arecibo beams.

Note that the equivalent H_2 column density N_{H_2} of the CNM1 are derived from H I data toward 3C132 and 3C133, a method different to the N_{H_2} of the L1544 envelope and core that are derived from dust emission. Therefore, in addition to the statistical errors listed in Table 1, there is a systematic difference between the N_{H_2} derived from the two methods. Considering that the regime traced by dust emission can be different from those traced by H I NSA or OH, which is particularly noticeable from the different spacial extents of dust and H I NSA in Fig. 1a, we expect that the systematic difference could be as large as a factor of a few. Since the values of λ between

CNM1 and L1544 are different at least by a factor of 13, the systematic difference between the two methods should not change the qualitative conclusion of this work.

In Fig. 1a, the peak of HiNSA column density appears to be shifted from the center of L1544 by 0.15 pc and the 70% and 90% contours of the peak HiNSA column density do not enclose L1544. We note that such offset has also been seen for other dense gas tracers in prestellar cores⁴¹. The core geometry may not be as simple as envisioned in idealized theories, where the dense core sits near the center of a lower density molecular envelope. In particular, the L1544 core appears to sit near one end of an elongated molecular (and dust) ridge, which roughly coincides with the region traced by HiNSA. Such an offset can result from complexities in chemistry and formation history, but does not affect the main science result of this work, namely, HINSA Zeeman probes the magnetic fields of current molecular ridge that is the progenitor of the dense core.

Maximum likelihood We adopt the analysis of maximum likelihood¹⁸ to study the uniformity of magnetic fields in the envelope of L1544. Assuming that the true B_{los} follows a gaussian distribution with mean B_0 and intrinsic spread σ_0 , the likelihood l_j for a single observation in a set of N measurements ($j = 1, \dots, N$) to measure B_j with gaussian error σ_j is proportional to the convolution of the probability $\exp[-(B - B_0)^2/2\sigma_0^2]/\sqrt{2\pi}\sigma_0$ for the magnetic field to have a true value of B with the probability $\exp[-(B - B_j)^2/2\sigma_j^2]/\sqrt{2\pi}\sigma_j$ of observing a value B_j of the field. Therefore, l_j is the integral over all possible true values of the magnetic field

$$l_j = \int_{-\infty}^{\infty} dB \frac{\exp[-(B - B_j)^2/2\sigma_j^2]}{\sqrt{2\pi}\sigma_j} \frac{\exp[-(B - B_0)^2/2\sigma_0^2]}{\sqrt{2\pi}\sigma_0}. \quad (7)$$

While the overall likelihood \mathcal{L} for a set of observations is the product of individual like-

likelihoods of the observations ($\mathcal{L} = \prod_{j=1}^N l_j$), the B_0 and σ_0 can be estimated by maximizing the likelihood \mathcal{L} . After performing the integration in Equation (7) and some algebraic manipulations,

$$\mathcal{L}(B_0, \sigma_0) = \left(\prod_{j=1}^N \frac{1}{\sqrt{\sigma_0^2 + \sigma_j^2}} \right) \exp \left[-\frac{1}{2} \sum_{j=1}^N \frac{(B_j - B_0)^2}{\sigma_0^2 + \sigma_j^2} \right]. \quad (8)$$

Extended Data Figure 1 shows the distribution of \mathcal{L} as functions of B_0 and σ_0 and the probability distributions of B_0 and σ_0 by integrating \mathcal{L} along the B_0 axis and the σ_0 axis, respectively. The probability distribution of B_0 is similar to a normal distribution with a mean value of $+4.1 \mu\text{G}$ and a standard deviation of $1.6 \mu\text{G}$. The probability distribution of σ_0 is highly asymmetric since the values of σ_0 cannot be negative. The first, second, and third quartiles of the σ_0 distribution are 0.6, 1.2, and $2.4 \mu\text{G}$. We therefore suspect that the Zeeman measurements in the L1544 envelope can be explain by a magnetic field with $B_0 = +4.1 \pm 1.6 \mu\text{G}$ and $\sigma_0 = 1.2_{-0.6}^{+1.2} \mu\text{G}$.

Inclination angle of magnetic field Given the uniformity of magnetic fields in the envelope of L1544 and CNM1 is well constrained by the maximum likelihood analysis, the coherent B_{los} suggests that the inclination angles of magnetic fields in the CNM1 and L1544 envelope are likely to be similar, or a special geometry of magnetic field structure across multi-scales and multi-phases of the interstellar medium is needed. In contrast, the B_{los} of the L1544 envelope and core differ by a factor of 2.6. There are two physical explanations for the 2.6-time difference between the HiNSA and OH Zeeman measurements. First, the OH measurement likely samples a denser gas than the HiNSA measurement, since the column density along the OH sightline is twice that along the HiNSA sightline (Table 1). Since the magnetic field strength in molecular clouds tends to increase with number density¹⁵, the stronger field is naturally expected in the denser core. Alternatively, the inclination angle of the L1544 core magnetic field could differ substantially from

that of the coherent field. Since we cannot rule out the second possibility, an assumption of similar inclination angles of the magnetic fields in the L1544 envelope and core thus is required in order to calculate the relative values of λ .

We note that dust polarization observation may give some clues since dust polarization traces position angle of the plane-of-sky component of magnetic field. The near-infrared polarization observations of L1544⁴² indicate that the mean position angle of magnetic field toward the core location of the Arecibo beam is 29.0° – 36.9° , and the mean position angles of magnetic fields toward the four envelope locations of the GBT beams are 30.5° – 55.8° . The difference of the position angles between the core and envelope thus may be about 10° – 20° .

We perform Monte Carlo simulations⁴³ to study whether the 2.6-time difference between the B_{los} of the L1544 envelope and core can be explained by different inclination angles. The simulations randomly generate two unit vectors in three dimensions, and then measure the difference between the inclination angles and the difference between the position angles of the two vectors. The probability of the cases that the line-of-sight length of one vector is 2.6-time larger than that of the other is ~ 0.19 . For those cases, the mean difference between the inclination angles and the mean difference between the position angles of the two vectors are about 38° and 45° , respectively. Since the probability of 0.19 is small and the difference of $\sim 45^\circ$ between the simulated position angles is about a factor of 2–4 larger than the difference of $\sim 10^\circ$ – 20° between the observed position angles, it is less likely that the 2.6-time difference between the B_{los} of the L1544 envelope and core can be solely explained by different inclination angles.

CCS Zeeman Measurements Ref. 20 reported a CCS Zeeman detection of $117 \pm 21 \mu\text{G}$ in a dense core of TMC-1 that has an estimated H_2 column density of $3 \times 10^{22} \text{ cm}^{-2}$, which is 4 times higher than that probed by OH Zeeman measurements in L1544 and nearly one order of magnitude higher than that probed by our HiNSA measurements. It appears to provide further support to the evolutionary scenario suggested by our HiNSA measurements: namely, once the gas loses its magnetic support during the transition from CNM to the molecular envelope (or ridge) and becomes magnetically supercritical, there is no longer any need to lose magnetic flux further (relative to the mass) in order for a piece of the envelope/ridge to condense into a (magnetically supercritical) core (e.g., the L1544 core probed by OH) and for the core to evolve further by increasing its column density (e.g., the TMC-1 core probed by CCS).

Technically, we note that one potential source of significant uncertainty in frequency shift, namely the uncertainty of beam squint, was not included in the CCS result, which may affect the level of significance. In comparison, the HiNSA measurement is robust with a $> 10\sigma$ significance with the beam squint and velocity gradient been taken into account by convolving the FAST Stokes V beam with the Stokes I cube of L1544 (see the third paragraph in the section of data reduction in Methods).

Data availability The data that support the findings of this study are openly available in Science Data Bank at <https://scidb.cn/en/s/VFRFnu>. FAST raw data are available from the <http://fast.bao.ac.cn> site one year after data-taking, per data policy of FAST. Due to the large data volume of this work and the speciality of polarization calibration, interested users are encouraged to contact the corresponding author to arrange data transfer. The reduced $I(\nu)$ and $V(\nu)$ spectra are available at

<https://github.com/taochung/HINSAzeeman>.

Code availability The codes analyzing the $I(\nu)$ and $V(\nu)$ spectra reported here are available at <https://github.com/taochung/HINSAzeeman>. The IDL RHSTK package is available at <http://w.astro.berkeley.edu/~heiles/>.

31. Jiang, P. et al. The fundamental performance of FAST with 19-beam receiver at L band. Res. Astron. Astrophys. **20**, 064 (2020).
32. Heiles, C. et al. Mueller Matrix Parameters for Radio Telescopes and Their Observational Determination. Publ. Astron. Soc. Pac. **113**, 1274–1288 (2001).
33. Jehle, M., Ruegg, M., Zuberbuhler, L., Small, D. & Meier, E. Measurement of Ionospheric Faraday Rotation in Simulated and Real Spaceborne SAR Data. EEE Trans. Geosci. Remote Sens. **47**, 1512–1523 (2009).
34. Perley, R. A. & Butler, B. J. Integrated Polarization Properties of 3C48, 3C138, 3C147, and 3C286. Astrophys. J., Suppl. Ser. **206**, 16 (2013).
35. McBride, J. & Heiles, C. An Arecibo Survey for Zeeman Splitting in OH Megamaser Galaxies. Astrophys. J. **763**, 8 (2013).
36. Peek, J. E. G. et al. The GALFA-H I Survey Data Release 2. Astrophys. J., Suppl. Ser. **234**, 2 (2018).

37. Ward-Thompson, D., Motte, F. & Andre, P. The initial conditions of isolated star formation - III. Millimetre continuum mapping of pre-stellar cores. Mon. Not. R. Astron. Soc. **305**, 143–150 (1999).
38. Griffin, M. J. et al. The Herschel-SPIRE instrument and its in-flight performance. Astron. Astrophys. **518**, L3 (2010).
39. Ossenkopf, V. & Henning, T. Dust opacities for protostellar cores. Astron. Astrophys. **291**, 943–959 (1994).
40. Roy, A. et al. Reconstructing the density and temperature structure of prestellar cores from Herschel data: A case study for B68 and L1689B. Astron. Astrophys. **562**, A138 (2014).
41. Lai, S.-P., Velusamy, T., Langer, W. D. & Kuiper, T. B. H. The Physical and Chemical Status of Pre-Protostellar Core B68. Astron. J. **126**, 311–318 (2003).
42. Clemens, D. P., Tassis, K. & Goldsmith, P. F. The Magnetic Field of L1544. I. Near-infrared Polarimetry and the Non-uniform Envelope. Astrophys. J. **833**, 176 (2016).
43. Hull, C. L. H. et al. Misalignment of Magnetic Fields and Outflows in Protostellar Cores. Astrophys. J. **768**, 159 (2013).

Acknowledgements This work is supported by the National Natural Science Foundation of China (NSFC) grant No. 11988101, U1931117, and 11725313; by CAS International Partnership Program No. 114A11KYSB20160008; by the National Key R&D Program of China No. 2017YFA0402600; and by the Cultivation Project for FAST Scientific Payoff and Research Achievement of CAMS-CAS. T.-C. C.

is funded by Chinese Academy of Sciences Taiwan Young Talent Program. Grant No.2018TW2JB0002. T.-C. C. and J. T. were supported by Special Funding for Advanced Users, budgeted and administrated by Center for Astronomical Mega-Science (CAMS), Chinese Academy of Sciences. C. H. is funded by Chinese Academy of Sciences President's International Fellowship Initiative Grant No. 2020DM0005. Z.-Y. L. is supported in part by NASA 80NSSC20K0533 and NSF AST-1716259 and 1815784. This work made use of data from FAST, a Chinese national mega-science facility built and operated by the National Astronomical Observatories, Chinese Academy of Sciences. This research has made use of the services of DSS2 survey of the ESO Science Archive Facility.

Author Contributions T.-C. C., D. L., and C. H. launched the FAST Zeeman project; T.-C. C. processed the data and analysis in consultation with C. H.; T.-C. C., Z.-Y. L., D. L., and C. H. drafted the paper; L. Q., Y. L. Y., and J. T. made key contributions to arrange the FAST observations of L1544 and polarization calibration; S. H. J. provided the H₂ column density map.

Competing Interests The authors declare that they have no competing financial interests.

Extended Data Table 1: **Gaussian Fit Parameters**

Component	I_{peak} [K]*	τ †	v_{LSR} [km s ⁻¹] ‡	σ_v [km s ⁻¹] §	B_{los} [μ G]	Order ‖
HiNSA	–	0.32 ± 0.01	6.97 ± 0.01	0.40 ± 0.01	$+3.8 \pm 0.3$	0
CNM1	90.34 ± 5.49	0.83 ± 0.12	8.12 ± 0.11	1.86 ± 0.05	$+4.0 \pm 1.1$	1
CNM2	116.33 ± 1.78	0.84 ± 0.08	-0.39 ± 0.33	2.41 ± 0.13	-7.6 ± 1.0	2
CNM3	135.31 ± 2.04	10.45 ± 0.95	4.38 ± 0.09	2.04 ± 0.06	$+2.9 \pm 0.4$	3
WNM	46.70 ± 2.47	–	2.63 ± 0.04	6.44 ± 0.09	-3.0 ± 1.7	4

* I_{peak} is the intrinsic peak Stokes I emission. We do not fit I_{peak} for HiNSA because it is an absorption component.

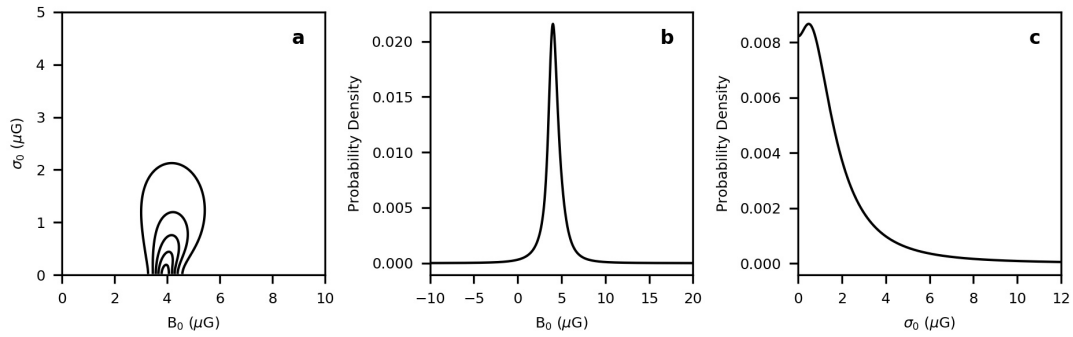
† τ is the central opacity. We do not fit τ for WNM because it is a background component.

‡ v_{LSR} is the central LSR velocity.

§ σ_v is the gaussian dispersion.

‖ The order of the component along the line of sight. Order begins with 0, and increasing numbers mean increasing distance along the line of sight. We fix order = 0 for HiNSA since Taurus cloud is one of the closest cloud to us.

The orders of the other components are free parameters in the fitting.



Extended Data Figure 1: Likelihood \mathcal{L} for the coherent magnetic field to have mean (B_0) and spread (σ_0) values. **a**, contours of \mathcal{L} as functions of B_0 and σ_0 plotted at 10%, 30%, 50%, 70%, and 90% of the peak value. **b**, the probability distribution of B_0 while allowing all possible values of σ_0 . **c**, the probability distribution of σ_0 while allowing all possible values of B_0 .